



Model for the cyclonic bias of convective vortices in a rotating system

Jenny Dingwall and John R. Taylor ^{*}

*Department of Applied Mathematics and Theoretical Physics, University of Cambridge,
Centre for Mathematical Sciences, Cambridge CB3 0WA, United Kingdom*

 (Received 19 September 2023; accepted 29 February 2024; published 26 March 2024)

In convective fluids, small vortices develop between neighboring convective cells. Familiar in the atmosphere in the form of dust devils and water spouts, these convective vortices have been seen in simulations of oceanic convection where the vortices exhibit an unexplained bias towards cyclonic rotation despite having a large Rossby number. Here we use large eddy simulations (LES) of an idealized oceanic convective mixed layer and vary independently the Coriolis acceleration and the surface buoyancy flux to investigate the development of the cyclonic bias of convective vortices. While large convective vortices are biased for sufficiently large values of the Coriolis parameter, small convective vortices do not exhibit a clear bias. Using Lagrangian particles, we find that the large convective vortices develop through the merger of many small convective vortices. We propose a statistical theory to predict the cyclonic bias of large convective vortices composed of many small unbiased convective vortices and test the theory using LES results. We apply the theory to typical convective conditions and find that convective vortices in upper ocean mixed layers are expected to exhibit a bias, while convective vortices in the terrestrial and Martian atmospheres are expected to be largely unbiased.

DOI: [10.1103/PhysRevFluids.9.033503](https://doi.org/10.1103/PhysRevFluids.9.033503)

I. INTRODUCTION

Thermal convection can occur when a fluid is heated from below or cooled from above, leading to an unstable density configuration. Convection is characterized by a regular, often hexagonal [1,2], pattern with narrow and intense convergent plumes surrounding large, weak areas of horizontally diverging fluid. Small “convective vortices” with a vertical axis of rotation develop in convective flows, particularly in the vertices joining two or more convective cells. In the terrestrial [3–5] and Martian atmosphere [4,6–8], convective vortices are sometimes made visible by entrained dust and sand and are commonly referred to as dust devils (or water spouts if they form over a body of water). On Earth, dust devils significantly increase the airborne transport of particles [9–13], which has potential to impact the weather and climate [14] or be hazardous to aircraft [15,16]. For similar reasons, Martian convective vortices with a high dust load could pose challenges towards future exploration of Mars [4]. Recent computational studies have observed convective vortices in the ocean surface boundary layer [17,18]. Here convective vortices trap buoyant material such as microplastics and oil droplets which are preferentially accumulated in small clusters at the surface [17,18], with implications for marine life and safety [19–21].

*J.R.Taylor@damtp.cam.ac.uk

Published by the American Physical Society under the terms of the [Creative Commons Attribution 4.0 International](https://creativecommons.org/licenses/by/4.0/) license. Further distribution of this work must maintain attribution to the author(s) and the published article's title, journal citation, and DOI.

It is often assumed that planetary rotation does not have a direct influence on convection in boundary layers in the atmosphere and ocean [22–24]. The relative importance of the nonlinear advection and Coriolis terms in convective flows is set by the convective Rossby number, $\text{Ro}^* = |B_0|^{1/2} f^{-3/2} H^{-1}$, where B_0 is the surface buoyancy flux driving convection, f is the Coriolis parameter, and H is the height of the convective layer [25–28]. Laboratory and numerical experiments suggest that rotational effects become important when $\text{Ro}^* \lesssim 0.1$ – 0.7 [29–31]. The well-studied problem of turbulent, Rayleigh-Benard convection under steady rotation has revealed asymmetric behavior of cyclones and anticyclones [32–35]. However, symmetry-breaking largely arises in the case of rapid rotation and relatively small Rossby numbers ($\text{Ro}^* < 1$), whereas flows with larger Ro^* are typically dominated by convective plumes which do not display a bias [32]. In atmospheric convection for a height of $H = 1$ – 2 km, $\text{Ro}^* \simeq 10$ [25], and despite some initial debate [36,37], the general consensus is that there is no significant rotational bias for dust devils [4,38,39].

In the upper ocean when convection develops in the top 10–100 m [40] and the heat flux is $\mathcal{O}(100 \text{ W m}^{-2})$ [25], Ro^* typically ranges between 0.5 and 10. Surprisingly, Dingwall *et al.* [18] found a strong bias towards cyclonic convective vortices in simulations with $\text{Ro}^* = 2.6$. Similar reports of an unexpected rotational bias exist in other flows. For example, Frank *et al.* [41], Sutherland *et al.* [42] observed a bias in the rotation of buoyant plumes in experiments with a large Rossby number. By diagnosing the evolution of vorticity along particle paths, Dingwall *et al.* [18] found that vortex stretching amplifies the planetary vorticity to generate the observed cyclonic bias in relative vorticity. However, this approach was purely diagnostic. Here one of our primary objectives is to develop a prediction for the vorticity bias of convective vortices in terms of the bulk parameters of the flow.

In this study, we propose a mechanism to explain the rotational bias of convective vortices and make a prediction for the bias in terms of the bulk parameters of the flow. Throughout this study, we assume $f > 0$, which leads to a cyclonic bias (while $f < 0$ would give an anticyclonic bias). Our analysis is based on large eddy simulations (LES) of free convection in an idealized domain. LES has been used to investigate terrestrial [38,43], Martian [44–46], and oceanic [17,18] convective vortices.

II. LARGE EDDY SIMULATIONS

We use large eddy simulations to solve a low-pass filtered version of the nonhydrostatic incompressible Boussinesq Navier-Stokes equations (1) and (2) in terms of the low-pass-filtered velocity $\mathbf{u} = (u, v, w)$, low-pass-filtered pressure p , and buoyancy θ ,

$$\frac{\partial \mathbf{u}}{\partial t} + \mathbf{u} \cdot \nabla \mathbf{u} + \mathbf{f} \times \mathbf{u} = -\frac{1}{\rho_0} \nabla p + \nu \nabla^2 \mathbf{u} - \nabla \cdot \boldsymbol{\tau} + \theta \mathbf{k}, \quad (1)$$

$$\frac{\partial \theta}{\partial t} + \mathbf{u} \cdot \nabla \theta = \kappa_\theta \nabla^2 \theta - \nabla \cdot \boldsymbol{\lambda}. \quad (2)$$

Buoyancy is treated as a single scalar variable under the assumption of a linear equation of state and neglecting double diffusive effects. In Eq. (1), ρ_0 is the reference density, \mathbf{k} is the unit vector in the vertical direction, ν is the molecular viscosity, $\boldsymbol{\tau}$ is the subgrid-scale stress tensor, and $\mathbf{f} = (0, 0, f)$ is the Coriolis force accounting only for the vertical component of the angular velocity vector using the so-called traditional approximation. In reality, the horizontal component of Earth’s rotation may have an effect, particularly at low latitudes, but here we neglect the horizontal component to simplify the analysis and focus only on the influence of the vertical component of rotation on convective vortices. In Eq. (2), $\boldsymbol{\lambda}$ is the subgrid-scale scalar flux and κ_θ is the molecular diffusivity. Both $\boldsymbol{\tau}$ and $\boldsymbol{\lambda}$ are calculated using the anisotropic minimum dissipation model [47,48].

The simulations are configured to represent an idealized ocean surface boundary layer cooled from the top, and we report dimensional values that are typical of the ocean, but the idealization of our simulations makes the results more broadly relevant. The domain is 125 m in the horizontal directions with periodic boundary conditions and 120 m in the vertical. Convection is driven using a

constant buoyancy loss at the surface with values ranging between $B_0 = -4.24 \times 10^{-10} \text{ m}^2/\text{s}^3$ (about 1 Wm^{-2}) and $B_0 = -4.24 \times 10^{-7} \text{ m}^2/\text{s}^3$ (about 1000 Wm^{-2}), and a zero flux bottom boundary condition for buoyancy. A no-stress boundary condition is applied at the top and bottom of the domain where the vertical velocity is zero. The Coriolis parameter is varied from $f = 10^{-6} \text{ s}^{-1}$ to $f = 10^{-4} \text{ s}^{-1}$. Buoyancy is initialized with a mixed layer of depth 80 m (where $\partial\theta/\partial z = 0 \text{ s}^{-2}$) overlying a region with stable stratification ($\partial\theta/\partial z = 9 \times 10^{-6} \text{ s}^{-2}$). Velocity is initialized as random white noise with an amplitude of 10^{-4} m/s . The molecular viscosity is $\nu = 10^{-6} \text{ m}^2/\text{s}$ and the molecular diffusivity is $\kappa_\theta = 10^{-6} \text{ m}^2/\text{s}$ ($\text{Pr} = 1$), although both are small compared to the subgrid-scale terms and hence do not have a direct impact on the simulations. The Rayleigh number based on the molecular viscosity and diffusivity varies between $\text{Ra} = \mathcal{O}(10^{16})$ and $\text{Ra} = \mathcal{O}(10^{18})$. We neglect transient effects by starting our analysis after the simulated flow has reached a fully developed turbulent state (approximately 4 h). Time averages are calculated over one inertial period, starting after 4 h, which is sufficient time for convection to develop into a statistically steady state.

The numerical code uses a pseudospectral method to calculate derivatives in the horizontal directions and second-order finite differences for the vertical direction. The timestepping algorithm is a mixed implicit-explicit scheme using third-order Runge-Kutta and Crank-Nicolson methods. Further details of the code can be found in Taylor [49]. In all simulations, resolved fields are discretized on a $512 \times 512 \times 65$ grid. This gives a horizontal grid spacing of 0.25 m. The vertical grid spacing is variable between 0.95 and 2.57 m with higher resolution near the surface. The domain size is large enough to accommodate one at least one convective cell. Although the large-scale convective dynamics may be constrained by the box size, the focus of this study is on the small-scale vortices, for which we need high resolution. As discussed in Appendix A, the number, intensity, and bias of the convective vortices do not change with increasing domain size or resolution.

We also include 16000 noninertial Lagrangian surface particles advected with the surface horizontal velocity field and vertically fixed at the first grid point below the surface. These follow the simplified Maxey-Riley equations [50] with all terms except for flow advection and Brownian motion neglected. The particle equations of motion are

$$\mathbf{x}_p(t + dt) = \mathbf{x}_p(t) + \mathbf{u}(\mathbf{x}_p, t)dt + \mathbf{x}_{\text{sgs}}(\mathbf{x}_p, t), \quad (3)$$

$$\mathbf{x}_{\text{sgs},i} = \frac{\partial v_{\text{sgs}}}{\partial x_i}(\mathbf{x}_p, t)dt + \{2[v_{\text{sgs}}(\mathbf{x}_p, t)]_+\}^{\frac{1}{2}}d\xi_i, \quad (4)$$

where \mathbf{u} is the resolved velocity interpolated at the particle position and \mathbf{x}_{sgs} is the displacement due to subgrid-scale motion, although this only has a small effect on particle motion. In Eq. (4), the subscript i indicates the spatial dimension, v_{sgs} is the subgrid-scale viscosity interpolated at the particle position, $d\xi_i$ is Gaussian white noise with variance dt , and $(\cdot)_+ = \max(\cdot, 0)$. We interpolate the velocity onto the particle position using cubic B splines [51] and time-step the particle position using the third-order Runge-Kutta method alongside the main LES code. Details of particle initialization are given later in the text when particles are used.

In Fig. 1(a), distinct convective cells are visible where large areas of weak upwelling are surrounded by small areas of strong downwelling in a simulation with $f = 10^{-4} \text{ s}^{-1}$ and $B_0 = -4.24 \times 10^{-8} \text{ m}^2/\text{s}^3$ at $t = 16.5 \text{ h}$. A twofold structure can be seen with a spokelike pattern of small convective cells (horizontal scale approximately 25 m) in the upper portion of the convective layer [Fig. 1(a)], and larger convective cells (horizontal scale approximately 50 m) which penetrate deeper into the upper mixed layer [Fig. 1(b)]. This structure is consistent with similar simulations of the ocean [52] and atmosphere [53].

The pressure field highlights convective vortices as areas with a local pressure minima. The convective vortices can be grouped into two classes. Large convective vortices are found in the downwelling bands of large convective cells at the nodes between convective cells, and smaller convective vortices are seen populating the large- and small-scale downwelling bands. Similar convective vortices were reported for idealized simulations of a convective atmospheric boundary layer by Raasch and Franke [38]. The small convective vortices are short lived and extend to a depth

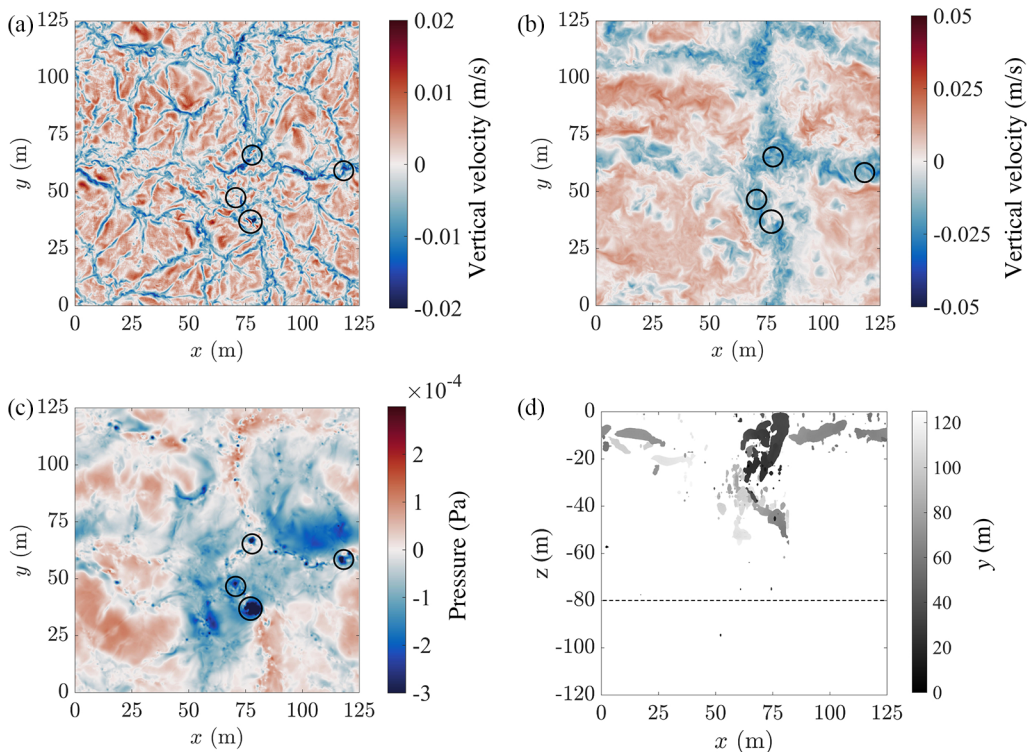


FIG. 1. Horizontal cross sections at $t = 16.5$ h of the vertical velocity at $z = -1$ m (a), vertical velocity at $z = -10$ m (b), pressure at $z = -1$ m (c), and a vertical cross section of pressure isosurfaces for $\delta_p < 3 \times \sigma_p$ Pa (d) in a simulation with $B_0 = -4.24 \times 10^{-8} \text{ m}^2/\text{s}^3$ and $f = 10^{-4} \text{ s}^{-1}$. Circles highlight locations of the largest four convective vortices [(a)–(c)] and the dashed line indicates the bottom of the mixed layer (d).

of about 5 m, while the large convective vortices are much more persistent and extend up to 40 m, which can be seen in Fig. 1(d), which shows a vertical cross section of pressure isosurfaces (see Appendix B for three-dimensional visualization).

Figure 2(a) shows the vertical vorticity field, ζ , averaged over the top 5 m (to reduce numerical noise near the surface) for the same B_0 , f , and t as in Fig. 1. The four convective vortices with the lowest pressure and largest area (circled) are all cyclonic but the small convective vortices show a roughly even mix of positive and negative vorticity.

We identify convective vortices following Dingwall *et al.* [18] based on algorithms used to detect dust devils in the atmosphere [38,43]. Specifically, we find the vortex center by identifying local minima in pressure and local maxima in the magnitude of filtered vorticity (we apply a Gaussian filter to the vorticity field to eliminate small-scale noise). Here local minima and maxima are defined as points where the pressure and vertical vorticity is smaller or larger than all points within a stencil of 15×15 neighboring grid points. This stencil size has been determined empirically to avoid detecting multiple vortex centers within one convective vortex. We use the pressure and vorticity fields evaluated at $z = -1$ m (the first grid cell below the surface) to ensure that the small, shallow vortices are captured. We additionally require the pressure minimum to be located within two horizontal grid points of the filtered vorticity maximum. The pressure minima must be less than 5 times the standard deviation of pressure ($p_{\max} < -5\sigma_p$) for the large convective vortices and between 0.5 and 5 times the standard deviation of pressure for the small convective vortices ($-5\sigma_p < p_{\max} < -0.5\sigma_p$). Similarly, we require the filtered vorticity extremum to be greater than 5 times the standard deviation of filtered vorticity ($|\zeta_{\max}| > 5\sigma_{\zeta}$) for the large convective vortices and

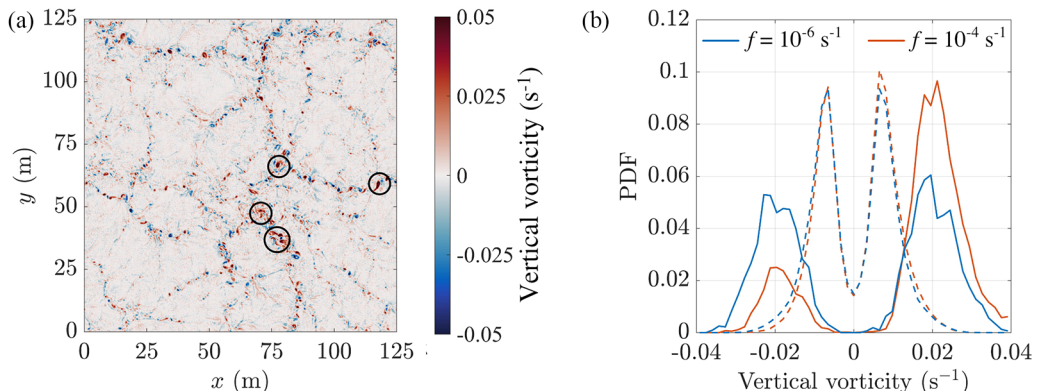


FIG. 2. (a) Horizontal cross sections at time $t = 16.5$ h of the vertical vorticity averaged over the top 5 m in a simulation with $B_0 = -4.24 \times 10^{-8} \text{ m}^2/\text{s}^3$ and $f = 10^{-4} \text{ s}^{-1}$. (b) Probability density function of vertical vorticity at $z = 0$ for points identified as large (solid) and small (dashed) convective vortices for $B_0 = -4.24 \times 10^{-8} \text{ m}^2/\text{s}^3$ and $f = 10^{-4} \text{ s}^{-1}$ (red) and $f = 10^{-6} \text{ s}^{-1}$ (blue).

between 2.5 and 5 times the standard deviation of filtered vorticity ($2.5\sigma_{\bar{\zeta}} < |\bar{\zeta}_{\max}| < 5\sigma_{\bar{\zeta}}$) for small convective vortices. Here the standard deviation for both pressure and filtered vorticity is calculated using horizontal cross sections taken at the analysis height and averaged over one inertial period. This threshold aims to eliminate as much noncoherent turbulence as possible, while still capturing sufficient information for analysis.

Figure 2(b) shows probability density functions (PDF) of ζ for two simulations with the same surface buoyancy flux but different values of f for all large and small convective vortices detected within one inertial period. To remove turbulent fluctuations, the vorticity at each vortex center is averaged over a 15×15 box (3.75×3.75) m centered at the vortex center. Both simulations exhibit a distinct peak at $\zeta = \pm 0.02 \text{ s}^{-1}$ for the large convective vortices (solid) and a peak at $\zeta = \pm 0.007 \text{ s}^{-1}$ for the small convective vortices (dashed). When $f = 10^{-4} \text{ s}^{-1}$ the large convective vortices have a distinct bias towards positive vorticity, but the distribution is relatively symmetric (with a slight positive bias) for the small convective vortices. When $f = 10^{-6} \text{ s}^{-1}$, the large convective vortices do not show a clear bias. The PDF for small convective vortices is very similar and nearly symmetric in both cases.

Our simulations reveal that the large convective vortices are composed of a large number of small convective vortices. We seed a collection of Lagrangian surface particles in a 5×5 m box inside each small convective vortex (both cyclonic and anticyclonic) detected by the algorithm at $t = 5$ h in a simulation with $B_0 = -4.24 \times 10^{-8} \text{ m}^2/\text{s}^3$ and $f = 10^{-4} \text{ s}^{-1}$ (when there is not a large vortex present) and track them until a large vortex forms at $t = 5.5$ h. Initially, the particles are distributed along the downwelling bands [Figs. 3(a) and 3(c)]. The small vortices quickly merge and particles accumulate in a much smaller area within the downwelling bands. As the vortices get closer to the node which joins nearby large-scale cells, they interact nonlinearly and eventually merge into one large vortex [Figs. 3(b) and 3(d)].

III. STATISTICAL THEORY FOR VORTICITY BIAS

Here we propose a statistical theory to quantitatively predict the cyclonic bias of the large convective vortices which is based on the observation above that large convective vortices are formed through the merger of many relatively unbiased small convective vortices. Statistically, the vorticity bias for large convective vortices can be predicted by averaging the absolute vorticity of many unbiased small convective vortices whose relative vorticity is sampled from an unbiased uniform distribution. Below we demonstrate this mechanism using simulations of idealized convective

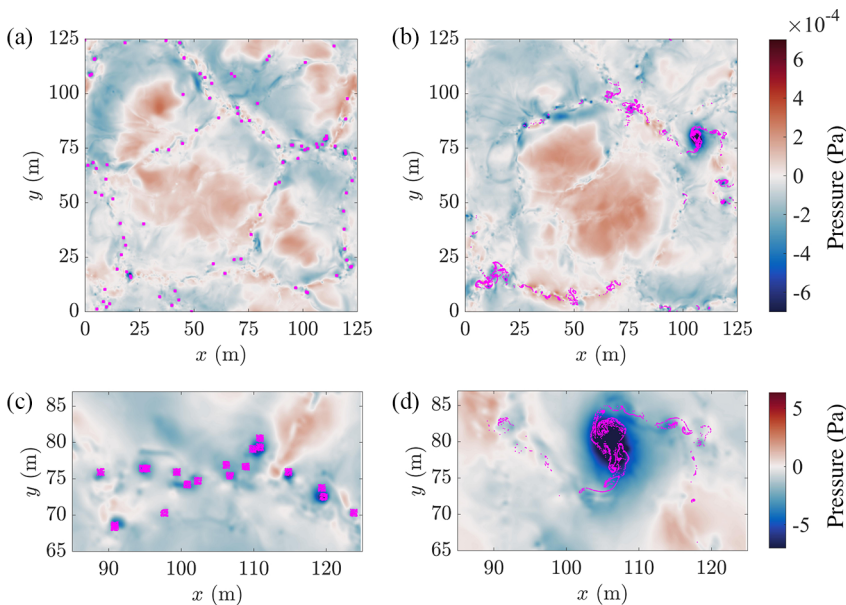


FIG. 3. Horizontal slices of pressure at $z = -1$ m with surface particle position (magenta) superimposed for $t = 5$ h [(a) and (c)] and $t = 5.5$ h [(b) and (d)]. Panels (c) and (d) show a zoomed in section of (a) and (b) containing the large convective vortex.

cells seeded with small random vortices. We then describe how to apply this prediction to forced convective flows using a scaling analysis and test it using the LES described above.

To explore the mechanism leading to a bias in the sign of the vorticity of the large convective vortices, we ran a suite of idealized LES, initialized with several overturning circulation cells superimposed with smaller vortices with random amplitude and an equal probability of cyclonic and anticyclonic vorticity. This simplified initial value problem allows us to control the structures and parameters in the flow much more closely and provides an ideal setting to introduce our mechanism and predictive analysis. The numerical method is the same as above, so here we only note changes and additions to those simulations. The initial vertical velocity is

$$w = w_0 \cos\left(\frac{4\pi x}{LX}\right) \cos\left(\frac{4\pi y}{LY}\right) \times \frac{-(z^2 + H_0 z)}{H_0} \quad (5)$$

in a $250 \times 250 \times 120$ m domain. This forms eight circulation cells, each of which mimic a convective cell. To model the small convective vortices, we superimpose a streamfunction composed of Gaussian vortices, each with radius $r = 2$ m and depth $d = 15$ m:

$$\psi = \sum_i \sum_j \xi_{ij} \exp\left[-\frac{(x-x_i)^2}{r^2} - \frac{(y-y_j)^2}{r^2}\right] \left(\frac{z+d}{d}\right), \quad (6)$$

where x_i and y_j denote the centers of the vortices and ξ_{ij} denotes the vorticity at the center of a given vortex, which is randomly sampled from a continuous uniform distribution on the interval $[-\xi, \xi]$. We systematically vary ξ and the Coriolis parameter, f . Since the convective cells are prescribed in the initial condition, we do not cool the surface and the surface buoyancy flux is $B_0 = 0$ m²/s³. Figure 4(a) shows the initial condition of small vortices with uniformly distributed amplitude when $\xi = 0.025$ m²/s and $f = 2 \times 10^{-5}$ s⁻¹. After $t = 0.8$ h, the small vortices have been advected towards the nodes joining neighboring circulation cells and the small vortices merge to form a large vortex. By design of the circulation cells, each large vortex has a distinct basin of

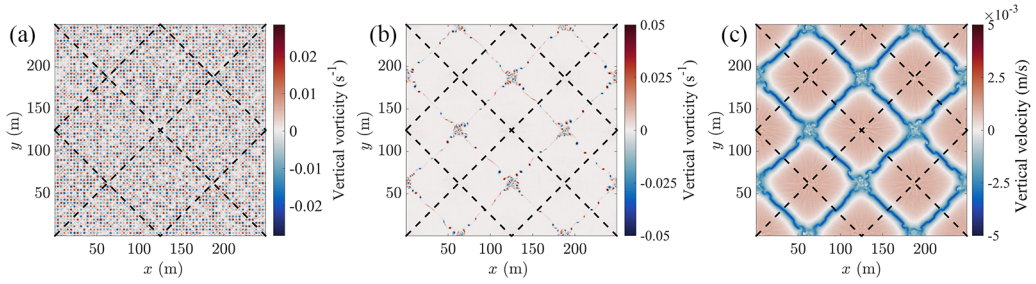


FIG. 4. Horizontal slice at $z = -1$ m of vertical vorticity when $t = 0$ h (a) and $t = 0.8$ h (b) and of vertical velocity when $t = 0.8$ h (c) with boundaries of basins of attraction superimposed (black dashed line) for $\xi = 0.025$ m²/s and $f = 2 \times 10^{-5}$ s⁻¹.

attraction (marked with a dashed black line). We focus on the time period from the start of the simulation until the large vortex forms at approximately 1 h. This ensures that the eight convective cells remain distinct and do not merge or interact with one another.

In order to quantify the change in vorticity as the small vortices merge into a large vortex, we seed Lagrangian surface particles at the center of each small vortex at the start of the simulation, and we track the vorticity along particle paths. The behavior of merging vortices is illustrated in Fig. 5

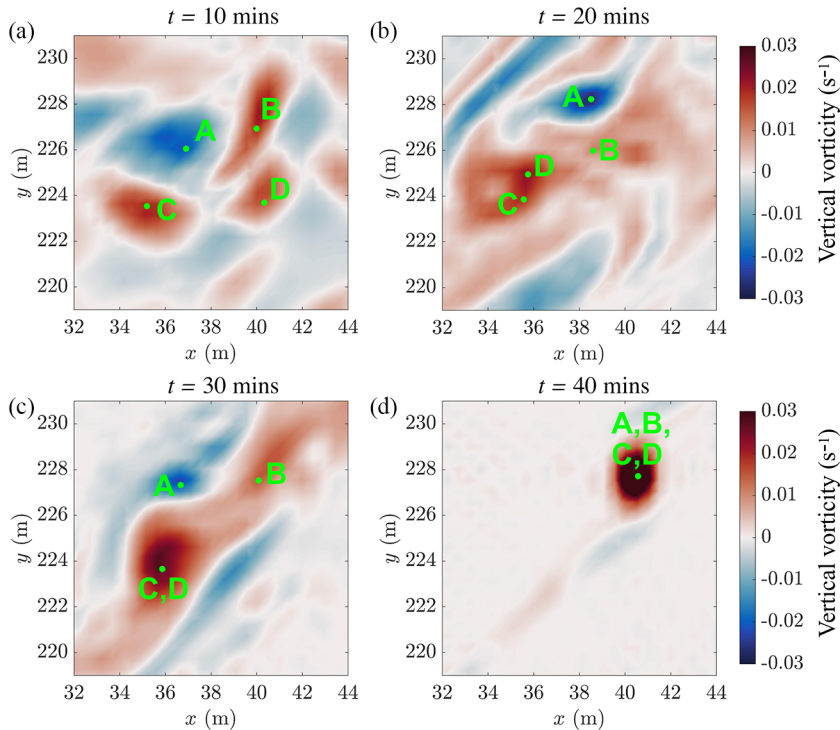


FIG. 5. Horizontal slices of vertical vorticity at $z = -1$ m with the position of four surface particles (A, B, C, and D) superimposed in a simulation with $\xi = 0.025$ m²/s and $f = 2 \times 10^{-5}$ s⁻¹ at $t = 10$ min, (a), $t = 20$ min, (b), $t = 30$ min, (c) and $t = 40$ min (d). The sequence shows the interaction and merging of four small vortices of opposing signs into one larger cyclonic vortex. In (c), particles C and D are at the same location and in (d) particles A, B, C, and D are all collocated.

which shows zoomed-in snapshots of the vertical vorticity field and tracks the position of four surface particles throughout the merger. Initially the particles are located at the center of four small Gaussian vortices (see Fig. 4 for the initial condition) of which three are cyclonic (with particles B, C, and D) and one anticyclonic (with particle A). By $t = 10$ minutes, the vortices begin to interact with one another [Fig. 5(a)], which results in the three small cyclonic vortices merging into one larger cyclonic vortex. The interaction distorts the anticyclonic vortex and causes it to reduce in size and strength [Figs. 5(b) and 5(c)]. Eventually, the cyclonic vortex envelopes the weaker anticyclonic vortex, so that by $t = 40$ min, all particles are contained inside a single, cyclonic vortex. This vortex is advected towards the node of the circulation cell and may undergo subsequent merging events.

At the stress-free upper surface ($z = 0$), the vertical component of the absolute vorticity ($\zeta + f$) satisfies:

$$\frac{D(\zeta + f)}{Dt} = (\zeta + f) \frac{\partial w}{\partial z} + \underbrace{\nu \nabla^2 \zeta}_{\zeta_{\text{diff}}}, \quad (7)$$

where D/Dt is the material derivative, w is the vertical velocity, and ν is the molecular diffusivity. The right-hand side comprises vortex stretching and diffusion. Hence, if diffusion is negligible and there are no vortex merging events, then the sign of the absolute vorticity is preserved along the particle paths. In the absence of vortex stretching, we might expect the vorticity of the large vortices to be small since the large vortices are formed through the merger of many small vortices with opposing sign. For example, in Fig. 5, the three cyclones and one anticyclone will still merge, but the resulting cyclonic vortex will be broader and weaker. Without vortex stretching, the vorticity would not increase in magnitude following the merger. Similarly, in a merger of three anticyclones and one cyclone (which is equally likely given our initial conditions), we could expect a broad and weak anticyclone to form. Because f does not play a role when there is no vortex stretching, the distribution of cyclones and anticyclones would be symmetric.

In our convective regime, the sign of $\partial w/\partial z$ can be both positive and negative, but it is positive in the downwelling regions where the large convective vortices are found. When $\partial w/\partial z > 0$, vortex stretching increases the magnitude of $\zeta + f$, leading to strong large vortices whose sign (after merging) is preserved. This effect can be seen in Fig. 5. The resultant cyclonic vortex contracts and its strength steadily increases between 20 and 40 min (at $t = 40$ min, the maximum vorticity is 0.08 s^{-1}). In the absence of any further mergers, this vortex remains cyclonic (since the sign of absolute vorticity is preserved) and vortex stretching continues to amplify its magnitude. Eventually, diffusion balances vortex stretching after the large vortex has formed. In a comparable merger between three anticyclones and one cyclone, the resultant vortex would initially have weak, negative vorticity. The magnitude of $\zeta + f$ would be smaller than the cyclonic case (since f is positive and ζ is negative) and so vortex stretching would be less effective at amplifying the vortex. If ζ were negative but very small (for example, if a larger number of small vortices merge), then $\zeta + f$ could be positive and amplification of $\zeta + f$ through vortex stretching could lead to a large cyclone, despite the vortex being composed of more anticyclones than cyclones.

Figure 6(a) shows statistics of the vorticity sampled along Lagrangian particle paths as a function of time for two cases with $\xi = 0.01 \text{ m}^2/\text{s}$ and $\xi = 0.025 \text{ m}^2/\text{s}$. The upper (and lower) quartile curves highlight the three stages by which small vortices merge into a large convective vortex: amplification of small vortices by vortex stretching (initial increase), nonlinear interactions between small vortices (slight decrease) followed by the amplification of the large vortex by vortex stretching (large increase). For both $\xi = 0.01 \text{ m}^2/\text{s}$ and $\xi = 0.025 \text{ m}^2/\text{s}$ the maximum positive vorticity of the 75th percentile is higher than the minimum negative 25th percentile due to the rotational bias of convective vortices (where particles are preferentially located), and the bias is larger for $\xi = 0.1 \text{ m}^2/\text{s}$. The small vortices begin to merge at about 0.6 h, after which there is a significant cyclonic bias [median line in Fig. 6(a)]. The cyclonic bias is weaker when the amplitude of the small vortices, ξ , is larger.

In our idealized simulations, the number of convective vortices that merge into a single large vortex is fixed by the initial condition, but we vary f and the amplitude of the small convective

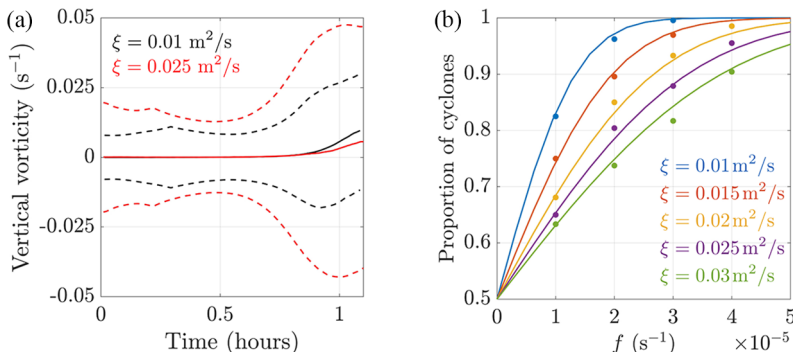


FIG. 6. (a) Median (solid) and 25th and 75th percentile (upper and lower dashed) particle vorticity when $\xi = 0.01 \text{ m}^2/\text{s}$ (black) and $\xi = 0.025 \text{ m}^2/\text{s}$ (red) for $f = 2 \times 10^{-5} \text{ s}^{-1}$. (b) The predicted proportion of cyclones versus f for different values of ξ (lines) and observed proportion of cyclones in simulations (points).

vortices (which we control using the parameter ξ). Since the sign of the absolute vorticity is conserved following particle paths (neglecting diffusion), we expect the sign of the absolute vorticity of the large vortex to be determined by the sign of the mean absolute vorticity of all small convective vortices from which it is composed. In our idealized simulations, we can calculate this by averaging the absolute vorticity over each basin of attraction at the start of the simulation. Since the relative vorticity of the small convective vortices is random and unbiased and since there are many small convective vortices in each basin of attraction, the mean absolute vorticity has a relatively small magnitude. However, vortex stretching amplifies the magnitude of the relative vorticity, and the simulations show that the relative vorticity of the large convective vortices is several orders of magnitude larger than the planetary vorticity, f . Hence the relative vorticity dominates the absolute vorticity of the large convective vortices, and the sense of rotation of the large convective vortices will be set by the sign of the mean absolute vorticity in each basin of attraction.

To test this hypothesis, we calculate the vorticity of large convective vortices in simulations for 18 different combinations of f and ξ . For each value of f and ξ , we run 30 simulations (which each have eight basins of attraction or large vortices) to ensure averaged results are statistically converged. In each case, we calculate the number of basins of attraction with cyclonic mean absolute vorticity and compare this with the number of large convective vortices with cyclonic rotation that develop in the simulation. Details of the calculation are described in Appendix C. The predicted proportion of cyclones [Fig. 6(b), lines] agrees very well with the proportion of cyclones observed (points) for different values of f and ξ . The predicted and simulated cyclonic bias is more prominent for larger values of f and smaller values of ξ . When f is small or ξ is large, the width of the probability distribution for the absolute vorticity averaged in each basin of attraction will be large compared to f , resulting in a weaker cyclonic bias. Due to nonlinear interactions between vortices, vortex stretching, and dissipation, not all individual regions preserve the sign of the mean absolute vorticity but the close agreement between our prediction and simulations in Fig. 6(b) suggests that, statistically, our prediction works very well.

The addition of many small convective vortices with a small bias in the absolute vorticity leads to a much more significant bias for the large convective vortices. Under this mechanism, the parameters which determine the bias are f , the vorticity of the small convective vortices and the number of small convective vortices that make up each large convective vortex. Changing f or the vorticity amplitude changes the initial the bias of the small convective vortices. Equally, the more small convective vortices that merge into a large vortex, the stronger we expect the bias to be.

This theoretical framework and the idealized LES can be used to predict the bias of convective vortices in the more realistic LES analyzed in the previous section. The bias of the large convective vortices is determined by the amplitude of the small vortices, ξ , the number of small vortices

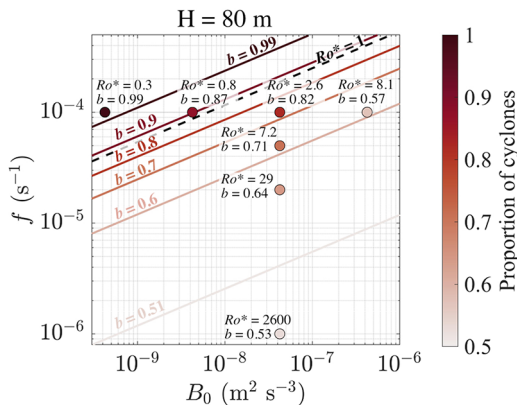


FIG. 7. Predicted probability contours (colored lines) and $Ro^* = 1$ line (black dashed) for constant H . We include Ro^* and the observed bias, b , for simulations (points).

contributing to each large vortex, and the Coriolis parameter, f . In the more realistic simulations, the number of small vortices feeding each large vortex is no longer fixed, and the vorticity of the small vortices is not controlled. We use scaling theory to relate these quantities to the bulk properties of the flow and apply the statistical theory described above.

The vorticity of the small convective vortices scales with B_0 and the depth of the convective layer, H , such that $\zeta \sim w^*/H$, where $w^* = (|B_0|H)^{1/3}$ is the convective velocity [54] (see Appendix D). When $|B_0|$ is large or H is small, the vorticity distribution has more extreme vorticity values so that $\zeta + f$ is less biased (equivalent to when ξ is large). To set the maximum amplitude of the small convective vortices, ξ , we use the upper limit set in our vortex detection algorithm, $\xi = 5 \text{ m}^2 \times \sigma_\zeta$. Empirically, we then find that $\xi = 260 \text{ m}^2 \times |B_0|^{1/3} H^{-2/3}$.

Based on the total number of small and large convective vortices detected from the LES, we find that on average there are 40 small vortices for every large convective vortex. Since the detection algorithm only identifies a small vortex when the vorticity is half of the maximum threshold, this is equivalent to 80 vortices with an amplitude that is randomly sampled from a uniform vorticity distribution. Here we model the statistics of the large convective vortices by averaging the vorticity of 80 small convective vortices, each randomly sampled from an unbiased uniform distribution with amplitude ξ . Applying this approach, we find that the vorticity distribution of the large convective vortices is well approximated by a Gaussian with mean $\mu = 0$ and standard deviation $\sigma = 3.4 \times 10^{-3} \text{ m}^{-2} \times \xi$, where ξ is the maximum vorticity of the small convective vortices. The sense of rotation of the large convective vortices is then set by the sign of the mean absolute vorticity of the 80 small vortices.

Figure 7 shows the proportion of large cyclonic convective vortices, with a convective layer depth of 80 m (typical of oceanic convection) for the theory (lines) and the LES (dots). The convective vortices show the largest bias for large f and small B_0 , a trend supported by both the simulations and theory. The mean-squared error of the points and lines in Fig. 7 is $MSE = 0.0054$.

IV. DISCUSSION AND SIGNIFICANCE

Here we built on previous work which showed that convective vortices can exhibit a significant rotational bias, even when Ro^* is large. In particular, we used large eddy simulations seeded with Lagrangian particles to analyze the development of a cyclonic bias in convective vortices. The convective vortices can be categorized into two types: small convective vortices, which are approximately equally distributed between cyclones and anticyclones, and large convective vortices, which exhibit a clear cyclonic bias. Our Lagrangian analysis shows that the large convective vortices

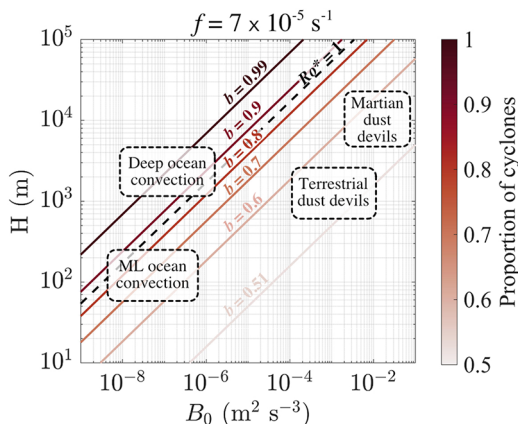


FIG. 8. Predicted probability contours (colored lines) and $Ro^* = 1$ line (black dashed) for constant f . We highlight the approximate parameter spaces for convective vortex regimes.

develop through the merger of many small convective vortices. We developed a statistical theory to predict the bias in the large convective vortices as a function of the bulk parameters of the flow.

We can apply the statistical theory to predict the bias in other settings. Figure 8 shows the approximate parameter space for convection in the terrestrial and Martian atmospheres and for shallow and deep ocean convection. In all cases we take $f = 7 \times 10^{-5} \text{ s}^{-1}$, although this is the lower end of f values for deep ocean convection which generally occurs in higher-latitude polar oceans. Below we provide further justification of the approximate ranges that B_0 and H take in the different convective regimes, which we summarize in Table I.

Observations and measurements of deep ocean convection are extensive and well reported. A cohesive review of typical deep ocean convective conditions is given in Marshall and Schott [25], and here we summarize the key values relevant to this study. Sites of deep ocean convection include the Labrador Sea, Greenland Sea, Mediterranean Sea and the Weddell Sea where the mixed layer depth, H , ranges from about 1000 to 4000 m. Typical values of the surface buoyancy flux range from $|B_0| = 10^{-6} - 10^{-8} \text{ m}^2/\text{s}^3$ where the corresponding heat loss can be between $Q = 100 - 1500 \text{ Wm}^{-2}$. For example, in the Mediterranean Sea, $H = 2000 \text{ m}$, $f = 10^{-4} \text{ s}^{-1}$, and $B_0 = -4 \times 10^{-8} \text{ m}^2/\text{s}^3$, giving $Ro^* = 0.3$. More generally, we can expect $Ro^* \sim 0.01 - 1$ in a deep convective regime.

Shallow mixed layer convection is typically characterized by a much smaller H and a smaller B_0 . For example, Chor *et al.* [17] used $H = 80 \text{ m}$ and a surface heat flux of $Q = 150 \text{ Wm}^{-2}$, while Mensa *et al.* [55] used $H = 50 \text{ m}$ and $Q = 1000 \text{ Wm}^{-2}$ to model convection in the ocean surface boundary layer. In this case, we estimate $Ro^* \sim 0.5 - 10$.

Heat fluxes in the terrestrial atmosphere are similar to those in oceanic convection because heat loss to the atmosphere drives convection in the ocean, but they have very different buoyancy fluxes. The ratio of the buoyancy fluxes in the ocean, B_{ocean} , and atmosphere, B_{atmos} , is written in Marshall

TABLE I. Typical parameters in different convective regimes.

Type of convection	$B_0 \text{ (m}^2/\text{s}^3)$	$H \text{ (m)}$	Ro^*
Deep ocean convection	$10^{-7} - 5 \times 10^{-7}$	1000–5000	0.01–1
Mixed layer ocean convection	$10^{-8} - 10^{-7}$	50–150	0.5–10
Terrestrial atmosphere	$10^{-3} - 5 \times 10^{-2}$	1000–2000	10–250
Martian atmosphere	$5 \times 10^{-3} - 10^{-1}$	5000–10 000	5–100

and Schott [25] as:

$$\frac{B_{\text{atmos}}}{B_{\text{ocean}}} = \frac{\rho_w c_w}{\rho_a \alpha c_a \theta_a} \approx 10^5, \quad (8)$$

where ρ is the density, c is the specific heat, α is the thermal expansion over water, and θ is the typical air temperature. Subscript w denotes water and a denotes terrestrial air. An estimate of the ratio is determined using typical meteorological values which suggests that the atmospheric buoyancy fluxes are about 10^5 times larger than oceanic buoyancy fluxes. This is consistent with Caughey [56] who estimate that $B_0 \approx 5 \times 10^{-3} \text{ m}^2/\text{s}^3$ in atmospheric boundary layer convection. The mixed layer depth in the terrestrial atmosphere is typically $H = 1000\text{--}2000$ m. Such parameters yield $\text{Ro}^* \sim 10\text{--}250$ in the terrestrial atmosphere.

Finally, Martian convection is similar to atmospheric convection but characterized by a larger H and larger B_0 . We can write

$$\frac{B_{\text{mars}}}{B_{\text{atmos}}} = \frac{\rho_a c_a \theta_a g_m}{\rho_m c_m \theta_m g_a} \approx 50, \quad (9)$$

where subscript m denotes Martian air and g is gravity. Again, the ratio is determined from typical Martian [57] and terrestrial [25] values. On Mars, the convective boundary layer can be up to 10 000 m [4], giving a similar range of Ro^* as in the atmosphere, $\text{Ro}^* \sim 5\text{--}100$.

Figure 8 shows that ocean mixed layer convection is expected to usually exhibit a cyclonic bias, consistent with Dingwall *et al.* [18], while deep oceanic convection is highly biased. Our theory predicts that most atmospheric regimes will be unbiased, with a slight rotational bias in Martian dust devils. This is consistent with observations and simulations of terrestrial dust devils [4,38], but Martian dust devil data are not yet extensive enough to test this prediction.

Finally, note that convective conditions often have additional sources of vorticity other than buoyancy flux, which may influence the derived scaling law. Examples include wind forcing [18], or bottom friction in the atmosphere, both of which have potential to increase vorticity fluctuations and inhibit the cyclonic bias. The rotational bias of convective vortices under more realistic conditions should be explored in future work.

APPENDIX A

The bias of convective vortices is independent of the simulation's horizontal resolution, Δx , vertical resolution, Δz , and horizontal domain size, L . To verify this, we run simulations varying L keeping $\Delta x = 1$ m and $\Delta z = 0.95\text{--}2.57$ m fixed (recall we use variable grid spacing in the z direction). Subsequently, we vary Δx and Δz keeping $L = 125$ m fixed. The additional simulations each have $B_0 = -4.24 \times 10^{-8} \text{ m}^2/\text{s}^3$, $f = 10^{-4} \text{ s}^{-1}$, and $H = 80$ m. To compare the vorticity distributions, we plot the vertical vorticity PDF at $z = -1$ m for points associated with convective vortices (using the vortex detection algorithm) and for all points in the domain. Note that the vortex detection algorithm applied here uses a larger detection radius than in the letter (5 m as opposed to 3.5 m in the letter) to ensure that vortices are captured in low-resolution, large domain simulations. A more detailed description of the method can be found in Dingwall *et al.* [18]. To remove turbulent fluctuations in the distribution for all points, the vorticity at each point is averaged over a box measuring 5×5 m.

Figures 9(a) and 9(b) shows the effect of varying the domain size (with $\Delta x = 1$ m and $\Delta z = 0.95\text{--}2.57$ m). For points associated with convective vortices (a), the peak remains at $\zeta \simeq \pm 0.015 \text{ s}^{-1}$ as the domain size decreases. The proportion of cyclones and anticyclones stays approximately the same with the most noticeable difference when $L = 62.5$ m. This is reflected in the distribution for all points, with again the most noticeable discrepancy between distributions when $L = 62.5$ m. For this reason, we choose to use a domain $L = 125$ m. At this size, there are only one or two large convective vortices at any given snapshot. However, we aim to resolve the small-scale motions as much as possible without adversely affecting the bias of convective vortices and we run simulations for a long-enough period of time for statistical quantities to converge.

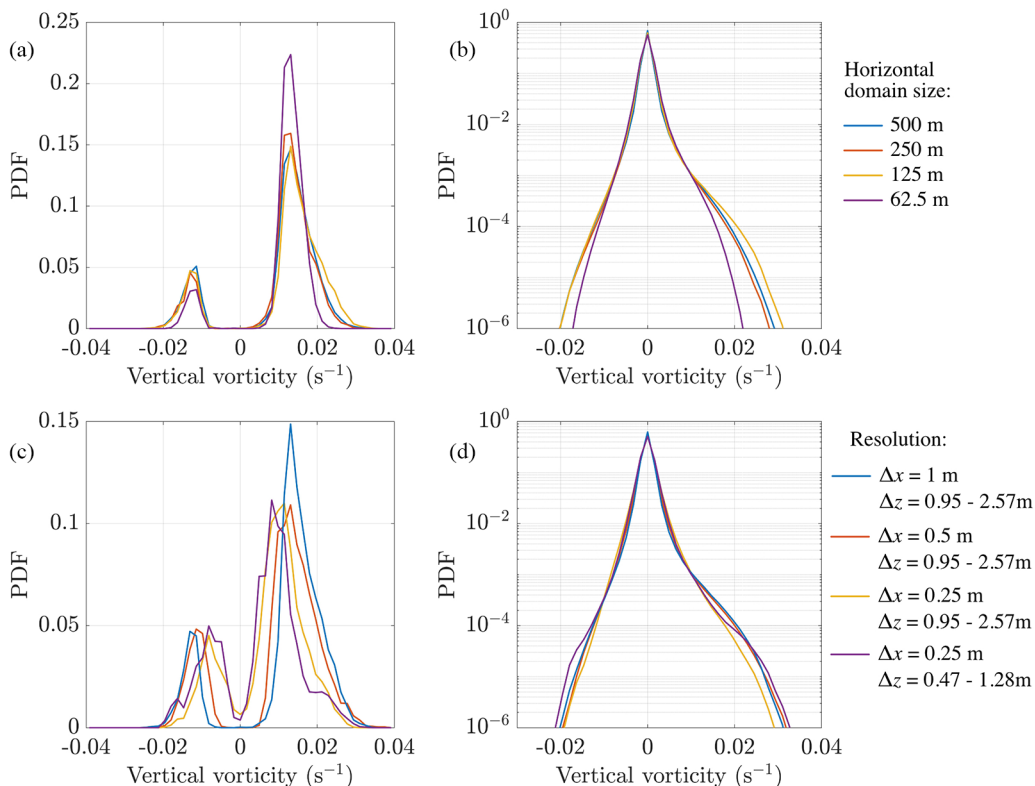


FIG. 9. Probability density function of vertical vorticity at $z = 0$ for points identified as convective vortices [(a) and (c)] and all points in the domain [(b) and (d)] as the domain size [(a) and (b)] and resolution [(c) and (d)] are varied.

Now with $L = 125$ m fixed, Figs. 9(c) and 9(d) shows the effect of increasing the horizontal resolution, Δx , and the vertical resolution, Δz . Again, the proportion of cyclones and the distribution for all points remain similar even for the highest-resolution simulations. We choose to use the highest computationally feasible resolution, $\Delta x = 0.25$ m and $\Delta z = 0.95$ – 2.57 m, to capture the small-scale convective vortices described in this study. When $\Delta x = 0.25$ m, the vortex detection algorithm detects more convective vortices with a near-zero vorticity. In the main text, we use a smaller detection radius in the algorithm to avoid this.

APPENDIX B

Figure 10 depicts a more detailed visualization of the small and large convective vortices from a simulation with $B_0 = -4.24 \times 10^{-8} \text{ m}^2/\text{s}^3$, $H = 80$ m, and $f = 10^{-4} \text{ s}^{-1}$ at time $t = 10$ h. The small vortices are coherent structures which occur regularly throughout the domain and we observe a roughly equal number of cyclones and anticyclones. The small vortices extend to a depth of between 5 and 10 m while the large vortex in Fig. 10(b) [and highlighted in the white box in Fig. 9(a)] extends to a depth of about 40 m, and in this case is cyclonic.

APPENDIX C

Here we describe the specifics of the calculations used to predict the number of basins of attraction with cyclonic mean absolute vorticity and the number of large convective vortices with cyclonic rotation that develop in the idealized simulations, which are compared in Fig. 6.

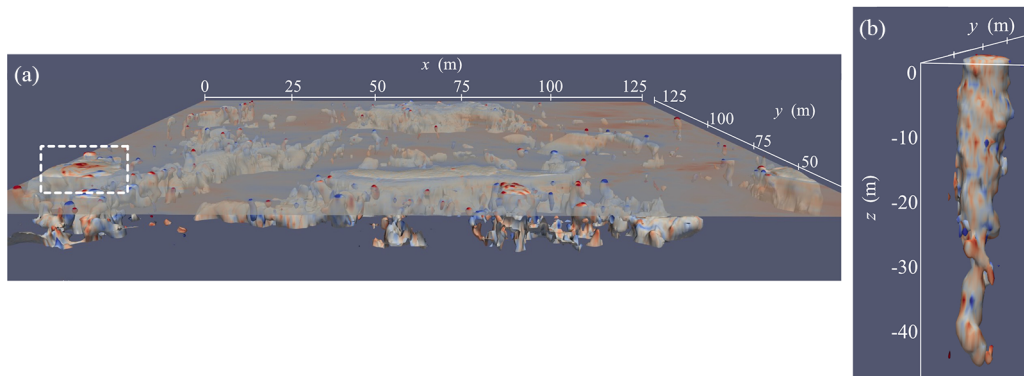


FIG. 10. Three-dimensional visualization of small (a) and large (b) convective vortices in a simulation with $B_0 = -4.24 \times 10^{-8} \text{ m}^2/\text{s}^3$ and $f = 10^{-4} \text{ s}^{-1}$. (a) The contour of perturbation pressure at $\delta p = \sigma_p$ up to a depth $z = -7 \text{ m}$ colored by vertical vorticity with a horizontal pressure slice overlain. (b) The contour of perturbation pressure at $\delta p = 5 \times \sigma_p$ colored by vertical vorticity for the large vortex highlighted in the white box in (a).

First, for any ξ and f , we calculate the mean vorticity within a single basin of attraction at $t = 0 \text{ h}$ (dashed square boxes in Fig. 4), $\overline{\zeta}_b$, where the overline denotes mean and subscript b denotes a quantity in an individual basin. Since the initial amplitude of the small vortices is uniformly distributed, several have a very small amplitude and we expect these to be quickly dissipated. We neglect such vortices by only considering points whose vorticity magnitude exceeds 20% of the vorticity standard deviation. Computing $\overline{\zeta}_b$ for each basin in each simulation, we find that the distribution of $\overline{\zeta}_b$ is well approximated by a Gaussian. An example of this approximation can be seen in Fig. 11 which shows the PDF of the initial mean basin vorticity, $\overline{\zeta}_b$, for all simulations with $\xi = 0.025 \text{ m}^2/\text{s}$. The distribution is very Gaussian (black dashed line shows a Gaussian with $\mu = 0$, $\sigma = 2.4 \times 10^{-5} \text{ s}^{-1}$). The Gaussian is symmetric about $\overline{\zeta}_b = 0$ by construction of uniformly distributed small vortices. Computing the standard deviation for all values of ξ and f , we find that the standard deviation linearly increases with ξ , with $\sigma = 0.978 \times 10^{-3} \text{ m}^{-2} \times \xi$, where the constant is determined empirically.

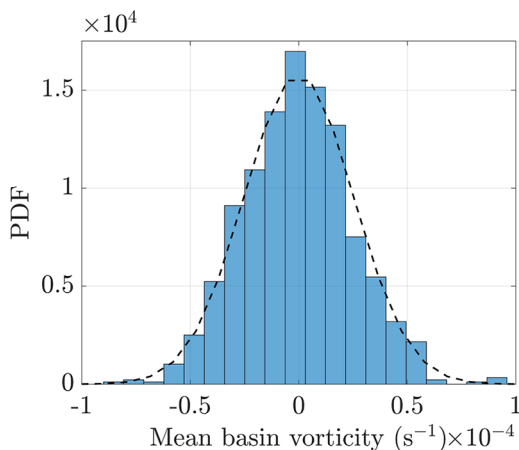


FIG. 11. PDF of initial mean basin vorticity for $\xi = 0.025 \text{ m}^2/\text{s}$ and Gaussian with $\mu = 0$, $\sigma = 2.4 \times 10^{-5} \text{ s}^{-1}$ (black dashed line).

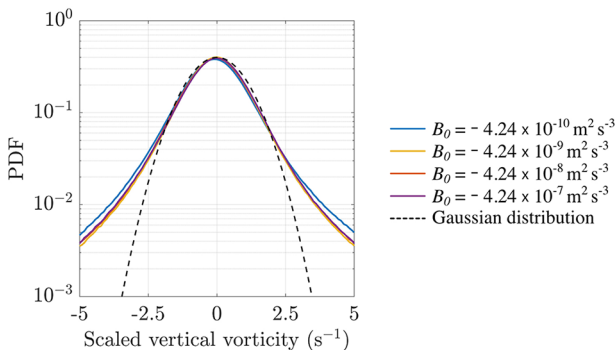


FIG. 12. Scaled probability density function of vertical vorticity in large-scale upwelling regions for simulations with $f = 10^{-4} \text{ s}^{-1}$ with a Gaussian approximation to the scaled curve (dashed line) at $z = -1 \text{ m}$.

While the distribution of initial relative vorticity, ζ , is symmetric about 0, the distribution of absolute vorticity, $\zeta + f$, is not. Accordingly, the distribution of $\bar{\zeta}_b + f$ is not symmetric about 0. To calculate the extent of the bias, we use the Gaussian approximation of $\bar{\zeta}_b$ and calculate the proportion of the distribution larger than $-f$ (the upper tail to the right of $-f$). This describes the probability of a basin of attraction initially having positive mean absolute vorticity, which we expect to determine whether a cyclone or anticyclone eventually forms. More specifically, we compute $P(Z > -f/\sigma)$ where Z is the standard normal distribution.

Second, in each test simulation, we determine whether a large cyclone or anticyclone has formed at the center of each basin of attraction later in the simulation once the small convective vortices have merged. We find the sign of the vertical vorticity field within radius 5 m of the center of the basin of attraction, averaged over a time interval $t = 0.875\text{--}0.925 \text{ h}$ (after the large vortex has formed but before dissipation of the large vortex ensues). If this is positive, then we judge that a cyclone has formed.

APPENDIX D

Empirically, the vorticity scales with B_0 and the depth of the convective layer, H , such that $\zeta \sim w^*/H$ where $w^* = (B_0 H)^{1/3}$. This scaling also holds in the shallow convective cells (which contain the small convective vortices) whose depth is a fraction of the convective layer depth. This scaling also holds in the shallow convective cells ($\zeta \sim w^*/h$) where h is the depth of the shallow convective cells. Typically, w^* characterizes the velocity scale in the upwelling region for a convectively driven flow. The area of the downwelling and upwelling regions is very asymmetric [Fig. 1(a)], and hence we expect a similar asymmetry between the upwelling and downwelling velocities. We can write this as $w_u = c w_d$ where subscript u denotes upwelling, d denotes downwelling, and c is a constant of asymmetry. Since the small convective cells are contained within the upwelling of large convective cells, there must be a point at the base of the small cell where the large-scale upwelling velocity balances the small-scale downwelling velocity, i.e., $W_u = w_u/c (= w_d)$. Rewriting this in terms of the relevant convective velocities gives $(|B_0|H)^{1/3} = (|B_0|h)^{1/3}/c$ and rearrangement yields $h/H = c^3$, i.e., the ratio of the depth of small and large convective cells is constant. To estimate the vorticity fluctuations in the small convective cells (and large-scale upwelling) which contain the small vortices, we use the relation $\zeta_u \sim |B_0|^{1/3} H^{2/3}$. Finally, note that the convective Rossby number can be rewritten in terms of ζ with a scaling constant, C , as $\text{Ro}^* = C(\zeta/f)^{3/2}$.

Figure 12 shows the scaled vertical vorticity pdf in the large-scale upwelling regions, i.e., $H^{2/3} \zeta_u / |B_0|^{1/3}$, for simulations with different values of B_0 but the same value of $f = 10^{-4} \text{ s}^{-1}$ and $H = 80 \text{ m}$, and the distributions collapse onto one another. The scaled distribution is relatively Gaussian for small vorticity values but has much wider tails. Studies of the non-Gaussian distribu-

tion of vorticity have previously suggested that the development of wide tails might be associated with vortex stretching of strong vortices [58,59], which in our case most likely relates to stretching of the large convective vortices.

-
- [1] F. Busse, Non-linear properties of thermal convection, *Rep. Prog. Phys.* **41**, 1929 (1978).
 - [2] P. J. Mason, Large-eddy simulation of the convective atmospheric boundary layer, *J. Atmos. Sci.* **46**, 1492 (1989).
 - [3] P. C. Sinclair, General characteristics of dust devils, *J. Appl. Meteor.* **8**, 32 (1969).
 - [4] M. Balme and R. Greeley, Dust devils on earth and mars, *Rev. Geophys.* **44**, 3 (2006).
 - [5] K. M. Kanak, Numerical simulation of dust devil-scale vortices, *Q. J. R. Meteorol. Soc.* **131**, 1271 (2005).
 - [6] M. D. Ellehoj, H. P. Gunnlaugsson, P. Taylor, H. Kahanpää, K. M. Bean, B. A. Cantor, B. T. Gheynani, L. Drube, D. Fisher, A. M. Harri, C. Holstein-Rathlou, M. T. Lemmon, M. B. Madsen, M. C. Malin, J. Polkko, P. H. Smith, L. K. Tamppari, W. Weng, and J. Whiteway, Convective vortices and dust devils at the phoenix mars mission landing site, *J. Geophys. Res.: Planets* **115**, E4 (2010).
 - [7] H. Kahanpää, C. Newman, J. Moores, M. P. Zorzano, J. Martín-Torres, S. Navarro, A. Lepinette, B. Cantor, M. T. Lemmon, P. Valentín-Serrano, A. Ullán, and W. Schmidt, Convective vortices and dust devils at the msl landing site: Annual variability, *J. Geophys. Res.: Planets* **121**, 1514 (2016).
 - [8] S. M. Metzger, J. R. Carr, J. R. Johnson, T. J. Parker, and M. T. Lemmon, Dust devil vortices seen by the mars pathfinder camera, *Geophys. Res. Lett.* **26**, 2781 (1999).
 - [9] D. A. Gillette and P. C. Sinclair, Estimation of suspension of alkaline material by dust devils in the united states, *Atmos. Environ. Part A* **24**, 1135 (1990).
 - [10] Y. Han, K. Wang, F. Liu, T. Zhao, Y. Yin, J. Duan, and Z. Luan, The contribution of dust devils and dusty plumes to the aerosol budget in western china, *Atmos. Environ.* **126**, 21 (2016).
 - [11] S. M. Metzger, M. R. Balme, M. C. Towner, B. J. Bos, T. J. Ringrose, and M. R. Patel, *In situ* measurements of particle load and transport in dust devils, *Icarus* **214**, 766 (2011).
 - [12] N. O. Renno, V. J. Abreu, J. Koch, P. H. Smith, O. K. Hartogensis, H. A. D. Bruin, D. Burose, G. T. Delory, W. M. Farrell, C. J. Watts, J. Garatuza, M. Parker, and A. Carswell, Matador 2002: A pilot field experiment on convective plumes and dust devils, *J. Geophys. Res.: Planets* **109**, E7 (2004).
 - [13] Y. Tang, Y. Han, and Z. Liu, Temporal and spatial characteristics of dust devils and their contribution to the aerosol budget in east asia-An analysis using a new parameterization scheme for dust devils, *Atmos. Environ.* **182**, 225 (2018).
 - [14] Y. Shao, K. H. Wyrwoll, A. Chappell, J. Huang, Z. Lin, G. H. McTainsh, M. Mikami, T. Y. Tanaka, X. Wang, and S. Yoon, Dust cycle: An emerging core theme in earth system science, *Aeolian Res.* **2**, 181 (2011).
 - [15] R. D. Lorenz and M. J. Myers, Local time (hrs) fraction of total dust devil hazard to aviation a review of united states air accident reports, *J. Meteorol.* **30** (2005), <https://api.semanticscholar.org/CorpusID:130933489>.
 - [16] R. D. Lorenz, Power law distribution of pressure drops in dust devils: Observation techniques and earth-mars comparison, *Planet. Space Sci.* **60**, 370 (2012).
 - [17] T. Chor, D. Yang, C. Meneveau, and M. Chamecki, A turbulence velocity scale for predicting the fate of buoyant materials in the oceanic mixed layer, *Geophys. Res. Lett.* **45**, 11,817 (2018).
 - [18] J. Dingwall, T. Chor, and J. R. Taylor, Large eddy simulations of the accumulation of buoyant material in oceanic wind-driven and convective turbulence, *J. Fluid Mech.* **954**, A27 (2023).
 - [19] M. Compá, C. Alomar, C. Wilcox, E. van Sebille, L. Lebreton, B. D. Hardesty, and S. Deudero, Risk assessment of plastic pollution on marine diversity in the mediterranean sea, *Sci. Total Environ.* **678**, 188 (2019).
 - [20] C. Wilcox, E. V. Sebille, B. D. Hardesty, and J. A. Estes, Threat of plastic pollution to seabirds is global, pervasive, and increasing, *Proc. Natl. Acad. Sci. USA* **112**, 11899 (2015).

- [21] E. V. Seville, C. Wilcox, L. Lebreton, N. Maximenko, B. D. Hardesty, J. A. V. Franeker, M. Eriksen, D. Siegel, F. Galgani, and K. L. Law, A global inventory of small floating plastic debris, *Environ. Res. Lett.* **10**, 12 (2015).
- [22] B. A. Klingler and J. Marshall, Regimes and scaling laws for rotating deep convection in the ocean, *Dyn. Atmos. Oceans* **21**, 227 (1995).
- [23] B. t. Morton, Geophysical vortices, *Prog. Aerosp. Sci.* **7**, 145 (1966).
- [24] G. Stubley and G. Riopelle, The influence of the earth's rotation on planetary boundary-layer turbulence, *Bound.-Layer Meteorol.* **45**, 307 (1988).
- [25] J. Marshall and F. Schott, Open-ocean convection: Observations, theory, and models, *Rev. Geophys.* **37**, 1 (1999).
- [26] R. Chen, H. J. Fernando, and D. L. Boyer, Formation of isolated vortices in a rotating convecting fluid, *J. Geophys. Res.* **94**, D15 (1989).
- [27] H. J. Fernando, R. R. Chen, and D. L. Boyer, Effects of rotation on convective turbulence, *J. Fluid Mech.* **228**, 513 (1991).
- [28] K. Julien, S. Legg, J. McWilliams, and J. Werner, Rapidly rotating turbulent rayleigh-bénard convection, *J. Fluid Mech.* **322**, 243 (1996).
- [29] T. Maxworthy and S. Narimousa, Unsteady, turbulent convection into a homogeneous, rotating fluid, with oceanographic applications, *J. Phys. Oceanogr.* **24**, 865 (1994).
- [30] M. Coates, G. Ivey, and J. Taylor, Unsteady, turbulent convection into a rotating, linearly stratified fluid: Modeling deep ocean convection, *J. Phys. Oceanogr.* **25**, 3032 (1995).
- [31] H. Jones and J. Marshall, Convection with rotation in a neutral ocean: A study of open-ocean deep convection, *J. Phys. Oceanogr.* **23**, 1009 (1993).
- [32] P. Vorobieff and R. E. Ecke, Turbulent rotating convection: An experimental study, *J. Fluid Mech.* **458**, 191 (2002).
- [33] C. Guervilly, D. W. Hughes, and C. A. Jones, Large-scale vortices in rapidly rotating Rayleigh-Bénard convection, *J. Fluid Mech.* **758**, 407 (2014).
- [34] B. Favier, L. J. Silvers, and M. R. Proctor, Inverse cascade and symmetry breaking in rapidly rotating boussinesq convection, *Phys. Fluids* **26**, 096605 (2014).
- [35] D. Sipp, E. Lauga, and L. Jacquin, Vortices in rotating systems: centrifugal, elliptic and hyperbolic type instabilities, *Phys. Fluids* **11**, 3716 (1999).
- [36] J. Durward, Rotation of 'dust devils', *Nature (Lond.)* **128**, 412 (1931).
- [37] H. B. Brooks, Shorter contributions: Rotation of dust devils, *J. Atmos. Sci.* **17**, 84 (1960).
- [38] S. Raasch and T. Franke, Structure and formation of dust devil-like vortices in the atmospheric boundary layer: A high-resolution numerical study, *J. Geophys. Res.* **116**, D16 (2011).
- [39] P. C. Sinclair, On the rotation of dust devils, *Bull. Am. Meteorol. Soc.* **46**, 388 (1965).
- [40] E. A. D'Asaro, Turbulence in the upper-ocean mixed layer, *Annu. Rev. Mar. Sci.* **6**, 101 (2014).
- [41] D. Frank, J. R. Landel, S. B. Dalziel, and P. F. Linden, Anticyclonic precession of a plume in a rotating environment, *Geophys. Res. Lett.* **44**, 9400 (2017).
- [42] B. R. Sutherland, Y. Ma, M. R. Flynn, D. Frank, P. F. Linden, D. Lemasquier, M. L. Bars, C. Pacary, T. Jamin, T. Dauxois, and S. Joubaud, Plumes in rotating fluid and their transformation into tornados, *J. Fluid Mech.* **924**, A15 (2021).
- [43] S. Giersch and S. Raasch, Evolution and features of dust devil-like vortices in turbulent Rayleigh-Bénard convection—A numerical study using direct numerical simulation, *J. Geophys. Res.: Atmos.* **126**, 7 (2021).
- [44] T. I. Michaels and S. C. Raffkin, Large eddy simulation of atmospheric convection on mars, *Q. J. R. Meteorol. Soc.* **130**, 1251 (2004).
- [45] A. Spiga, E. Barth, Z. Gu, F. Hoffmann, J. Ito, B. Jemmett-Smith, M. Klöse, S. Nishizawa, S. Raasch, S. Raffkin *et al.*, Large-eddy simulations of dust devils and convective vortices, *Space Sci. Rev.* **203**, 245 (2016).
- [46] S. Nishizawa, M. Odaka, Y. O. Takahashi, K.-I. Sugiyama, K. Nakajima, M. Ishiwatari, S.-I. Takehiro, H. Yashiro, Y. Sato, H. Tomita *et al.*, Martian dust devil statistics from high-resolution large-eddy simulations, *Geophys. Res. Lett.* **43**, 4180 (2016).

- [47] M. Abkar, H. J. Bae, and P. Moin, Minimum-dissipation scalar transport model for large-eddy simulation of turbulent flows, [Phys. Rev. Fluids](#) **1**, 041701(R) (2016).
- [48] C. A. Vreugdenhil and J. R. Taylor, Large-eddy simulations of stratified plane couette flow using the anisotropic minimum-dissipation model, [Phys. Fluids](#) **30**, 8 (2018).
- [49] J. R. Taylor, Numerical Simulations of the Stratified Oceanic Bottom Boundary Layer, Ph.D. thesis, University of California, San Diego (2008).
- [50] M. R. Maxey and J. J. Riley, Equation of motion for a small rigid sphere in a nonuniform flow, [Phys. Fluids](#) **26**, 883 (1983).
- [51] M. A. T. van Hinsberg, J. Thije Boonkamp, F. Toschi, and H. Clercx, On the efficiency and accuracy of interpolation methods for spectral codes, [SIAM J. Sci. Comput.](#) **34**, B479 (2012).
- [52] E. D. Skillingstad and D. W. Denbo, An ocean large-eddy simulation of langmuir circulations and convection in the surface mixed layer, [J. Geophys. Res.](#) **100**, 8501 (1995).
- [53] H. Schmidt and U. Schumann, Coherent structure of the convective boundary layer derived from large-eddy simulations, [J. Fluid Mech.](#) **200**, 511 (1989).
- [54] J. W. Deardorff, Numerical investigation of neutral and unstable planetary boundary layers, [J. Atmos. Sci.](#) **29**, 91 (1972).
- [55] J. A. Mensa, T. M. Özgökmen, A. C. Poje, and J. Imberger, Material transport in a convective surface mixed layer under weak wind forcing, [Ocean Model.](#) **96**, 226 (2015).
- [56] S. J. Caughey, Observed characteristics of the atmospheric boundary layer, in *Atmospheric Turbulence and Air Pollution Modelling* (Springer, Berlin, 1982), pp. 107–158.
- [57] P. Thomas and P. J. Gierasch, Dust devils on mars, [Science](#) **230**, 175 (1985).
- [58] S. B. Pope, *Turbulent Flows* (Cambridge University Press, Cambridge, UK, 2000).
- [59] M. Wilczek and R. Friedrich, Dynamical origins for non-gaussian vorticity distributions in turbulent flows, [Phys. Rev. E](#) **80**, 016316 (2009).